Thin-Walled Structures 173 (2022) 108960

Contents lists available at ScienceDirect

Thin-Walled Structures

journal homepage: www.elsevier.com/locate/tws

Full length article

First failure load of sandwich beams under transient loading using a space–time coupled finite element method

Devin J. Burns[1], R.C. Batra[1,*]

Department of Biomedical and Engineering Mechanics, Virginia Polytechnic Institute and State University, Blacksburg, VA, 24061, United States of America

ARTICLE INFO

Keywords:
Elastodynamics
Tsai–Wu failure criterion
ANOVA
First failure load
Sensitivity analysis

ABSTRACT

We numerically analyze transient plane stress deformations of linearly elastic laminates and sandwich structures by using a coupled space–time finite element method with the weak form of governing equations derived by the least-squares method. The governing equations are written as seven first-order partial differential equations as in the state space formulation, and each variable is approximated by using piece-wise continuous basis functions. The sum of the integral over the problem (space-time) domain of squares of residuals of the governing equations, and initial and boundary conditions is minimized with respect to the nodal values of the seven variables to deduce coupled linear algebraic equations. The developed software is verified by comparing computed results for sample problems with their either analytical or numerical solutions obtained with a commercial software, ABAQUS. Using statistical method and the Tsai–Wu failure criterion, sensitivities of the maximum deflection and the first failure load to beam's aspect ratio (AR), the facesheet-core thickness ratio (FCTR), and the facesheet-core in-plane and transverse stiffness ratios (FCISR, FCTSR) are elucidated. For sandwich beams with equal FCISR and FCTSR, the results are sensitive to the AR and the FCTR. In general, they strongly depend upon the FCTSR and its interaction with the AR and the FCTR.

1. Introduction

As composite materials have become more ubiquitous in structural applications, the need to understand and accurately predict their behavior in complex loading environments has increased. Due to their high specific strength and stiffness ratios, sandwich panels are frequently used in aerospace, civil and marine applications. In particular, sandwich structures made with stiff facesheets and a soft core material dissipate significant amount of energy through plastic core compression, transverse shear deformations and bending, which make them well suited for blast mitigation applications [1].

Numerous works have studied the dynamic and blast mitigating behavior of composite structures. These may be categorized into experimental, analytical, or numerical studies of a composite's response to an impulsive/transient loading. Experimental works on blast mitigation typically involve the detonation of a charge, either in air or underwater, at various distances from the target subjected to different geometries, materials, and boundary conditions. Wanchoo et al.'s review paper discusses the historical and the current state-of-the-art experimental works on blast-mitigating composite structures [2]. Because such experiments are often time consuming and expensive, it is highly desirable, and often necessary, to develop analytical or computational methods for simulating the transient response of composite structures to dynamic loads.

Closed form, or exact, solutions for the three-dimensional (3D) linear elasticity theory equations (LETE) for transient deformations of laminates and sandwich structures are scarce. Challenges in solving problems for heterogeneous bodies like sandwich composite beams and plates include accurately finding transverse stresses that cause delamination between adjacent layers and satisfying interlaminar continuity conditions [3]. For simply supported laminated plates deformed statically, the 3D LETE have been solved by expressing the three displacements as double Fourier series in the in-plane coordinates and deducing ordinary differential equations for them in the thickness direction [4–6]. For more general boundary conditions at the edges, Vel and Batra [7,8] employed the Eshelby–Stroh formalism and satisfied boundary conditions at the edges in the sense of Fourier series that rely on St. Venant's principle [9,10]. Demasi [11] has provided exact solutions for 2D and 3D static bending deformations of thick and thin sandwich plates by first casting the governing equations in the state-space formulation, and then using eigenvectors and generalized eigenvectors as the basis functions.

Another common approach for finding exact solutions is the state space method in which the three transverse stresses and the three

* Corresponding author.
E-mail address: rbatra@vt.edu (R.C. Batra).
[1] Both authors equally contributed to the work.

https://doi.org/10.1016/j.tws.2022.108960
Received 16 November 2021; Received in revised form 10 January 2022; Accepted 16 January 2022
Available online xxxx

displacements are taken as variables, and the LETE are written as first-order partial differential equations (PDEs) in the thickness coordinate, z. The boundary value problem is thus reduced to one that looks like an initial value problem and is solved by finding a propagation matrix that relates the variables for two different values of z (see [12,13]). The state-space approach was used by Khdeir and Reddy to find exact solutions for the transient response of simply-supported symmetric cross-ply laminates [14]. For anisotropic structures subjected to blast loading, Song et al. and Librescu et al. used the Laplace transform method to predict transient deformations and stresses in thin-walled beams and sandwich composite panels [15,16]. Transient problems for heterogeneous media are analyzed in Refs. [17–20].

In many engineering situations, deformations and/or stresses within a structure may be assumed to correspond to either plane strain or plane stress thereby reducing the problem to 2D. The pressurization of a very long homogeneous cylinder is an example of plane strain deformations, while a state of plane stress occurs in the thin skin of an aircraft where stresses through the skin's thickness are assumed to be negligible. Ding et al. derived analytical solutions for fixed–fixed isotropic and anisotropic beams subjected to uniform surface loading by using the Airy stress function [21,22]. A similar method was also employed in [23] for functionally graded anisotropic beams, where material properties, body forces and the stress function were assumed to be functions of the thickness coordinate. Ren presented a closed-form solution to the generalized plane strain problem for a cantilevered anisotropic plate [24] by assuming a particular form for the displacements which ensured satisfaction of continuity conditions at material interfaces.

Nearly all practical engineering problems involve arbitrary geometries, loading and boundary conditions, and cannot be analytically analyzed. They are, therefore, numerically studied by generally employing the finite element method (FEM), e.g. see [25,26]. In this paper, we employ the state-space formulation of the plane stress problem, express the 7 unknown fields in terms of the FE basis functions defined on the spatial and the time domains, find residuals of the governing equations and the initial and the boundary conditions, integrate squares of these residuas over the space–time domain, and derive algebraic equations for the coefficients of the basis functions by minimizing the sum of squares of the residuals. This approach has been called the least squares FEM (LSFEM), and has been employed among others by Surana et al. for studying 1D wave propagation in periodically laminated composites [27], Pontaza and Reddy to find displacements and stress-resultants in shear-deformable isotropic shells [28], and Moleiro et al. to analyze static deformations and free vibrations of multi-layered composite plates [29].

Advantages of the LSFEM include incorporation of the initial and the boundary conditions into the problem formulation, and the use of higher-order FE basis functions in the time domain. Its shortcoming is the large size of the resulting simultaneous algebraic equations whose solution can take considerable computational time, and require large storage space. The technique is implicit and is generally unconditionally stable. However, the solution accuracy may require the use of small time steps. For piecewise linear FE basis functions in the time domain the technique becomes the traditional time-marching scheme. Mathematical concepts of the space–time FEs are discussed in [30,31]. One could use Hamilton's principle to derive governing equations in terms of nodal displacements and nodal accelerations, and then use the FEM in the time domain to deduce algebraic equations for nodal displacements at discrete values of time, e.g., see [32]. It requires using either Lagrange multipliers or penalty parameters to satisfy continuity conditions at interfaces between two abutting layers of different materials.

We use the Tsai–Wu failure criterion [33] to ascertain the first failure load (FFL) of sandwich composite beams, and the statistical method, ANOVA, to determine how sensitive the FFL is to typical design parameters like the beam's aspect ratio (AR), the facesheet-core thickness ratio (FCTR) and the facesheet-core in-plane and transverse stiffness ratios (FCISR, FCTSR). The importance of considering the FCTSR in studying free vibrations of sandwich structures, and delineating the load transfer between the facesheets and the core in static deformations is elucidated in [33].

The novelties of this work include (i) demonstrating that polynomial basis functions defined on the entire spatial domain (i.e., one FE along the beam length) can simulate stress wave propagation in sandwich composite structures, and (ii) statistically determining beam design parameters that most affect the FFL according to the Tsai–Wu failure criterion.

The remainder of the paper is structured as follows. Section 2 describes the transient plane stress problem studied and derives the state-space form of the governing equations. Discrete equations for the associated space–time FEM including initial and boundary conditions derived by minimizing the squares of the residuals for the FE basis functions are given in Section 3. Numerical examples and results for a few problems including the parameter sensitivity study are provided in Section 4. Conclusions of the work are summarized in Section 5.

2. Problem formulation

Consider a sandwich beam of total thickness h, length L and unit width with boundary $\partial\mathscr{B}$ occupying the region $\mathscr{B}$ in the reference configuration in the x_1x_3-plane as depicted in Fig. 1. The beam is constructed with a core material bounded by two stiff facesheets each of thickness h_f and the core of thickness h_c. All layers are assumed to be made of a linearly elastic, homogeneous, and transversely isotropic material, with the axis of transverse isotropy along the x_1-axis, and are perfectly bonded to each other. The x_1-axis is in the beam's mid-plane and the beam extends from $-\frac{h}{2}$ to $+\frac{h}{2}$ in the x_3-direction. The temporal evolution of the beam occurs in the time interval $[0,T]$, with T being the final time of interest. Therefore, the complete space–time domain occupied by the kth layer ($k = 1,2,3$) is $\Omega^k X [0,T]$, where Ω^k is the region of space in the reference configuration occupied by the kth layer at time $t = 0$.

2.1. Governing equations

In a multilayered beam with perfectly bonded layers, surface tractions and displacements must be continuous across an interface between two adjoining layers. These are usually called the interface continuity conditions, and for a 3-layer sandwich beam undergoing plane stress deformations in the x_1x_3-plane they are

$$\begin{aligned} &\sigma^k_{13_t} = \sigma^{k+1}_{13_b}, \qquad \sigma^k_{33_t} = \sigma^{k+1}_{33_b}, \qquad k = 1,2,\\ &u^k_{1_t} = u^{k+1}_{1_b}, \qquad u^k_{3_t} = u^{k+1}_{3_b}, \qquad k = 1,2, \end{aligned} \tag{1}$$

where u_i denote the displacements in the x_i-direction, σ^k_{ij} the components of the stress tensor σ with respect to the x_1-, x_2- and x_3-axes and subscripts t and b denote the top and the bottom surfaces of the kth layer, respectively.

To simultaneously solve for stresses and displacements in the beam we use a state-space formulation. Furthermore, to approximate the unknown variables using C^0 basis functions, the governing PDE's are written to include at most first-order derivatives. Accordingly, we define the axial and the transverse velocities, respectively, as

$$v^k_1 = \frac{\partial u^k_1}{\partial t}, \qquad v^k_3 = \frac{\partial u^k_3}{\partial t}. \tag{2}$$

The balance of linear momentum for the kth layer is

$$\begin{aligned} &\frac{\partial \sigma^k_{11}}{\partial x_1} + \frac{\partial \sigma^k_{13}}{\partial x_3} + f^k_1 - \rho^k \frac{\partial v^k_1}{\partial t} = 0,\\ &\frac{\partial \sigma^k_{13}}{\partial x_1} + \frac{\partial \sigma^k_{33}}{\partial x_3} + f^k_3 - \rho^k \frac{\partial v^k_3}{\partial t} = 0. \end{aligned} \tag{3}$$

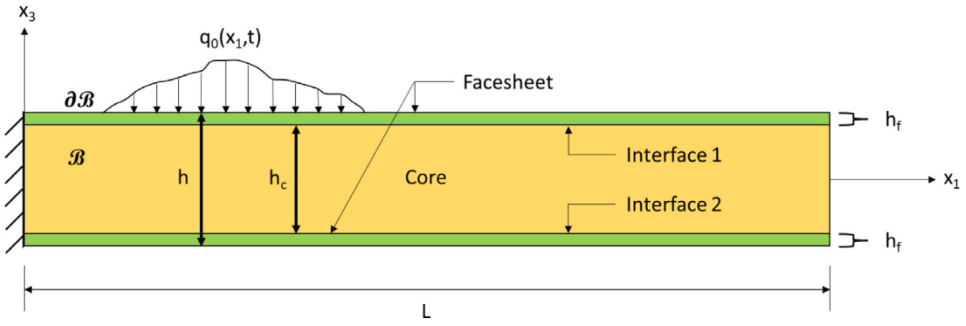

Fig. 1. Rectangular Cartesian coordinate system and geometry for a cantilevered sandwich beam with boundary conditions.

In Eqs. (3), the f_i^k $(i = 1, 3)$ denote the body force components, along the x_i-axis, per unit volume, and ρ^k the material mass density.

Since σ_{11} need not be continuous at the layer interfaces, we eliminate it from Eq. $(3)_1$ and rewrite it in terms of only layer-wise continuous variables. A similar approach was used by Bahar in [12] and Moleiro et al. [29] for analyzing static deformations and free vibrations of multilayered plates. The constitutive relation in the Voigt notation of the kth layer material is

$$\begin{aligned} &\sigma_\alpha^k = \overline{C}_{\alpha\beta}^k \epsilon_\beta^k, \qquad \alpha, \beta = 1, 2, \ldots, 6, \\ &\sigma = \left\{\sigma_{11}, \sigma_{22}, \sigma_{33}, \sigma_{23}, \sigma_{13}, \sigma_{12}\right\}, \quad \epsilon = \left\{\epsilon_{11}, \epsilon_{22}, \epsilon_{33}, 2\epsilon_{23}, 2\epsilon_{13}, 2\epsilon_{12}\right\} \end{aligned} \tag{4}$$

where $\overline{C}_{\alpha\beta}^k = \overline{C}_{\beta\alpha}^k$ are elastic constants transformed from the material principal coordinate axes to the problem coordinates, and $\sigma_\alpha^k = 0$ for $\alpha = 2, 4, 6$ for plane stress deformations.

In Eq. (4), $\epsilon_{11}, \epsilon_{22}, \ldots$ are components of the infinitesimal strain tensor that are related to displacements by

$$\epsilon_{ij} = \frac{1}{2}\left(\frac{\partial u_i}{\partial x_j} + \frac{\partial u_j}{\partial x_i}\right), \quad i, j = 1, 2, 3. \tag{5}$$

We use $\sigma_{22} = \sigma_{23} = \sigma_{12} = 0$ in Eq. (4) to express ϵ_{22}, ϵ_{13} and ϵ_{33} in terms of ϵ_{11} and σ_{33}, and substitute the result into the expression for σ_{11} to obtain

$$\begin{aligned} &\epsilon_{33}^k = \hat{C}_{36}^k \sigma_{33}^k - \hat{C}_{46}^k \epsilon_{11}^k, \\ &2\epsilon_{13}^k = \frac{\sigma_{13}^k}{\hat{C}_{44}^k}, \\ &\sigma_{11}^k = \hat{C}_{11}^k \epsilon_{11}^k + \hat{C}_{13}^k \sigma_{33}^k. \end{aligned} \tag{6}$$

Expressions for $\hat{C}_{\alpha\beta}^k$ in terms of $\overline{C}_{\alpha\beta}^k$ are given in Appendix A, and for the $\overline{C}_{\alpha\beta}^k$ in terms of engineering constants for a transversely isotropic material in Appendix B. Substituting for σ_{11}^k from Eq. $(6)_3$ into Eq. $(3)_1$ gives

$$\hat{C}_{11}^k \frac{\partial \epsilon_{11}^k}{\partial x_1} + \hat{C}_{13}^k \frac{\partial \sigma_{33}^k}{\partial x_1} + \frac{\partial \sigma_{13}^k}{\partial x_3} + f_1^k - \rho^k \frac{\partial v_1^k}{\partial t} = 0. \tag{7}$$

We note that if a layer is made of an isotropic material, the terms $\hat{C}_{11}^k$ and $\hat{C}_{13}^k$ are modified but the form for Eq. (7) remains the same.

The constitutive relation (4) is rewritten as follows by differentiating both sides with respect to time, t, and assuming that the material elasticities do not vary with time.

$$\begin{aligned} &\frac{\partial \sigma_\alpha^k}{\partial t} = \overline{C}_{\alpha\beta}^k \frac{\partial \epsilon_\beta^k}{\partial t}, \\ &\frac{\partial \epsilon_{ij}}{\partial t} = \frac{1}{2}\left(\frac{\partial v_i}{\partial x_j} + \frac{\partial v_j}{\partial x_i}\right), \quad i, j = 1, 2, 3. \end{aligned} \tag{8}$$

Note that for infinitesimal deformations being studied here one does not need to use total time derivatives in Eq. (8). Following a similar procedure as with the stress–strain relationships, we write the out-of-plane and layer-wise discontinuous velocity gradients in terms of the x_1x_3-plane components. Using Eqs. (8), we arrive at the following stress-rate velocity-gradient constitutive equations,

$$\begin{aligned} &\frac{\partial \sigma_{13}^k}{\partial t} - \hat{C}_{44}^k \frac{\partial v_1^k}{\partial x_3} - \hat{C}_{44}^k \frac{\partial v_3^k}{\partial x_1} = 0, \\ &\frac{\partial \sigma_{33}^k}{\partial t} - \hat{C}_{31}^k \frac{\partial v_1^k}{\partial x_1} - \hat{C}_{33}^k \frac{\partial v_3^k}{\partial x_3} = 0. \end{aligned} \tag{9}$$

Eq. $(8)_2$ for $i = 1, j = 1$ is written as

$$\frac{\partial \epsilon_{11}^k}{\partial t} - \frac{\partial v_1^k}{\partial x_1} = 0. \tag{10}$$

The complete system of governing coupled partial differential equations then consists of Eqs. (2), $(3)_2$, (7), (9) and (10) for the seven unknowns,

$$\mathbf{s} = \left[\sigma_{13} \quad \sigma_{33} \quad \epsilon_{11} \quad v_1 \quad v_3 \quad u_1 \quad u_3\right]^T. \tag{11}$$

We define below the kinetic and the strain energies that are used to compare solutions from the present approach with those computed using ABAQUS.

$$\mathscr{K}(t) = \frac{1}{2}\int_0^L \int_{-\frac{h}{2}}^{\frac{h}{2}} \rho^k \left(v_1^k v_1^k + v_3^k v_3^k\right) dx_3 dx_1, \tag{12}$$

$$\mathscr{S}(t) = \frac{1}{2}\int_0^L \int_{-\frac{h}{2}}^{\frac{h}{2}} \left(\sigma_{11}^k \epsilon_{11}^k + 2\sigma_{13}^k \epsilon_{13}^k + \sigma_{33}^k \epsilon_{33}^k\right) dx_3 dx_1. \tag{13}$$

Comment: In Eqs. (12) and (13), please delete summation form k = 1 to N before the integral sign.

2.2. Initial and boundary conditions

We assume that the body is at rest and is stress free at time $t = 0$. The time interval $[0, T]$ is divided into n time intervals not necessarily of the same size. The residuals for initial conditions for the time interval $[t_{i-1}, t_i]$ are written as:

$$R_{a_{in}}^k \equiv s_a^{-k}(x_1, x_3, t_{i-1}) - s_a^{+k}(x_1, x_3, t_{i-1}), \quad (a = 1, 2, \ldots, 7),$$

where "+" (-) indicates the value at the end (start) of the time step $[t_{i-2}, t_{i-1}]$ ($[t_{i-1}, t_i]$). We note that these residuals are identically zero for the exact solution, but are typically non-zero when expressions for approximate solutions are substituted in them.

We presume that surface tractions are applied on the beam's top and bottom surfaces. The edges at $x_1 = 0, L$ are either clamped, free or simply-supported. Residuals for the boundary conditions at the edge $x_1 = 0$ are listed below.

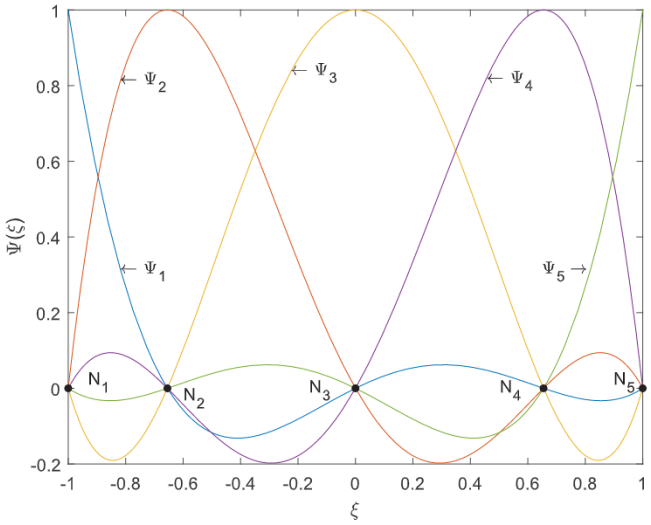

Fig. 2. Legendre–Gauss–Lobatto shape functions for a 5-node master element along the ξ-axis.

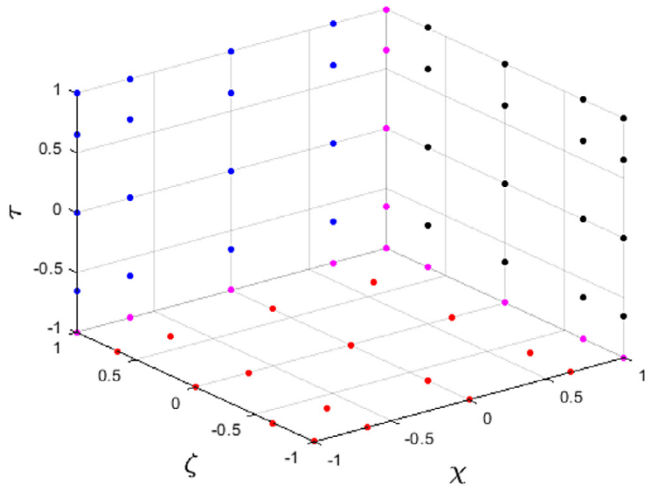

Fig. 3. Locations of $5 \times 5 \times 5$ nodes on the three bounding faces of a master element.

Clamped:

$$R^k_{bc_1} \equiv u^k_1(0, x_3, t), \quad R^k_{bc_2} \equiv u^k_3(0, x_3, t), \quad (k = 1, 2, 3),$$

Free:

$$R^k_{bc_3} \equiv \sigma^k_{11}(0, x_3, t), \quad R^k_{bc_4} \equiv \sigma^k_{13}(0, x_3, t), \quad (k = 1, 2, 3),$$

Simply-supported:

$$R^k_{bc_5} \equiv \sigma^k_{11}(0, x_3, t), \quad R^k_{bc_6} \equiv u^k_3(0, x_3, t), \quad (k = 1, 2, 3).$$

REsiduals for the boundary conditions on the top surface are:

$$R^3_{bc_7} \equiv \sigma^3_{13}(x_1, x_3^{top}, t) - \hat{q}^+_1(x_1, t), \quad R^3_{bc_8} \equiv \sigma^3_{33}(x_1, x_3^{top}, t) - \hat{q}^+_3(x_1, t).$$

Surface tractions prescribed on the bottom surface are denoted by $\hat{q}^-_1$ and $\hat{q}^-_3$ and residuals for them can be written as those for the top surface.

2.3. Tsai–Wu failure criterion

Predicting where and when a composite structure will fail is important. Here, we use the Tsai–Wu failure criterion (see [33]) for the facesheets and the core. For a state of plane stress, failure occurs when the failure index $F \geq 1$, where

$$F = F_1\sigma_{11} + F_3\sigma_{33} + F_{11}\sigma^2_{11} + F_{33}\sigma^2_{33} + F_{55}\sigma^2_{13} + 2F_{13}\sigma_{11}\sigma_{33}, \tag{14}$$

and

$$F_1 = \frac{1}{X_T} - \frac{1}{X_C}, \quad F_3 = \frac{1}{Z_T} - \frac{1}{Z_C}, \quad F_{11} = \frac{1}{X_T X_C}, \quad F_{33} = \frac{1}{Z_T Z_C}, \quad F_{55} = \frac{1}{S^2}, \quad F_{13} = -\frac{1}{2}\frac{1}{\sqrt{X_T X_C Z_T Z_C}}. \tag{15}$$

In Eqs. (14) and (15), we have dropped the superscript "k" for the kth layer. X_T and Z_T (X_C and Z_C) are the tensile (compressive) strengths along the material principal directions, S is the in-plane shear strength and stresses in Eq. (14) must be relative to the material principal coordinate axes.

We do not perform a progressive failure analysis where the material elasticities are reduced upon failing. Rather, we only find the time (or the load) when a material point in the beam first fails. The expression in Eq. (14) is used for both materials at an interface to check if a material point has failed at that interface. Delamination is not studied in this paper.

The primary reason for using the Tsai–Wu failure criteria is that values of five strength parameters are available in the literature for the composites studied herein. Other failure criteria, e.g., Hashin's [34], and Puck and Schürmann's [35] can easily be employed. The computed FFL will depend upon the failure criterion but other results presented herein are independent of it.

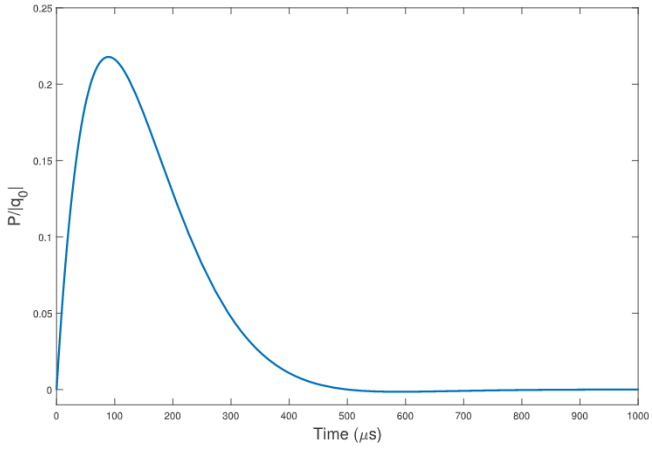

Fig. 4. Time history of the applied surface traction for Sections 4.1.2, 4.2 and 4.3 given by Eq. (24).

3. Weak formulation using the least-squares method

In this section, we derive the discrete form of Eqs. (2), (3)$_2$, (7), (9) and (10) and the associated initial and boundary conditions by minimizing the sum of the squares of their residuals, which is referred to as the least-squares method. Unknown field variables in the kth layer are approximated as

$$S^k_m(x_1, x_3, t) = \sum_{i=1}^{P_{x_1}} \sum_{l=1}^{P_{x_3}} \sum_{n=1}^{P_t} A^k_{m_{iln}} \Phi_i(x_1)\Psi_l(x_3)\Lambda_n(t), \quad m = 1, 2, \ldots, 7, \tag{16}$$

where Φ_i, Ψ_l and Λ_n are C^0 basis functions in the x_1, x_3 and t-directions, respectively, and P_{x_1}, P_{x_3} and P_t are integers. We construct the following functional in which the integration is over the space–time domain with time in the interval $[t_{i-1}, t_i]$,

$$J(\sigma_{13}, \sigma_{33}, \epsilon_{11}, v_1, v_3, u_1, u_3) = J_\Omega + J_{in} + J_{bc}, \tag{17}$$

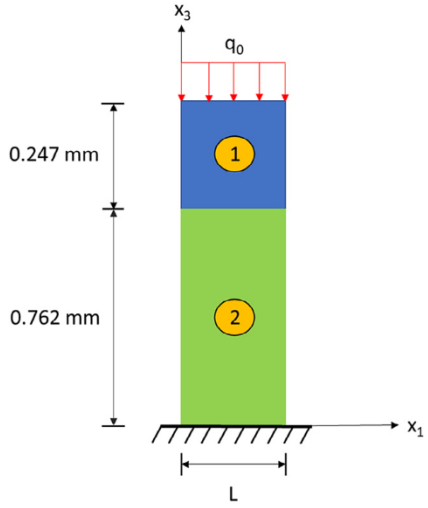

Fig. 5. Pressure pulse problem geometry (dimensions used are the same as in [27]).

$$J_{\Omega} = \frac{1}{2}\sum_{m=1}^{7}\sum_{k=1}^{3}\int\int\int R_m^k R_m^k dx_3 dx_1 dt, \tag{18}$$

$$J_{in} = \frac{1}{2}\sum_{m=1}^{7}\sum_{k=1}^{3}\int\int R_{in_m}^k R_{in_m}^k dx_3 dx_1 dt. \tag{19}$$

Note that the continuity of surface tractions and displacements at an interface between two adjoining layers are identically satisfied in this work. For a cantilever beam clamped at $x_1 = 0$ with surface tractions prescribed only on the top surface,

$$\begin{aligned} J_{bc} = {} & \frac{1}{2}\sum_{k=1}^{3}\int\int\left(\left(R_{bc_1}^k R_{bc_1}^k + R_{bc_2}^k R_{bc_2}^k\right)\Big|_{x_1=0}\right. \\ & \left. + \left(R_{bc_3}^k R_{bc_3}^k + R_{bc_4}^k R_{bc_4}^k\right)\Big|_{x_1=L}\right) dx_3 dt \\ & + \frac{1}{2}\sum_{k=1}^{3}\int\int\left(\left(R_{bc_7}^k R_{bc_7}^k + R_{bc_8}^k R_{bc_8}^k\right)\Big|_{x_3=\frac{h}{2}}\right) dx_1 dt \\ & + \frac{1}{2}\sum_{k=1}^{3}\int\int\left(\left(R_{bc_7}^k R_{bc_7}^k + R_{bc_8}^k R_{bc_8}^k\right)\Big|_{x_3=-\frac{h}{2}}\right) dx_1 dt. \end{aligned} \tag{20}$$

Substituting from Eq. (16) into Eq. (17) and evaluating the integrals gives J as a function of the $7 \times P_{x_1} \times P_{x_3} \times P_t$ variables $A_{m_{iln}}^k$ per layer. Necessary conditions for J to be stationary are

$$\frac{\partial J}{\partial A_{m_{iln}}^k} = 0. \tag{21}$$

We note that in the traditional FEM, one generally uses the finite-difference method to march forward the nodal values of displacements in time. Explicit algorithms using lumped mass matrices do not require solving a set of simultaneous algebraic equations for nodal displacements for every discrete value of time. Even though the time step dictated by the stability condition is quite small, large size problems involving millions of unknowns can be analyzed. In the method used herein, Eq. (21) results in a set of algebraic equations whose solution provides values of unknowns at all nodes in the space and time domains. The method is implicit, and for several nodes on an element in the time domain, it requires solving for a huge number of unknowns making it unsuitable for analyzing large size problems.

3.1. Discrete formulation

We discretize each space–time layer domain into N_{x_1} and N_t not necessarily uniform finite elements (FEs) along the x_1- and the t- axes, respectively. Thus, P_{x_1}, P_{x_3} and P_t equal the number of nodes along the x_1-, x_3- and t- axes, respectively. We find a continuously differentiable one-to-one mapping onto a master cube $[-1,1]\times[-1,1]\times[-1,1]$ for each element in the x_1x_3t-space.

For an element having p nodes along the x_1-axis, we find their images on the master element $[-1,1]$. In terms of the natural coordinate, ξ, on $[-1,1]$, the p shape functions are taken as

$$\Psi_i(\xi) = \frac{(\xi-1)(\xi+1)L_p'(\xi)}{p(p+1)L_p(\xi_i)(\xi-\xi_i)}, \tag{22}$$

where Ψ_i denotes the shape function for node i, a prime indicates differentiation with respect to ξ and $L_p(\xi)$ is a Legendre polynomial of order p. For a master element with five nodes, the Ψ_i's are complete polynomials of degree four, and are shown in Fig. 2. Nodal coordinates are roots of $\Psi_i(\xi) = 0$ and are generally called the Legendre–Gauss–Lobatto (LGL) points when also used as integration points. We have shown in Fig. 3 the distribution of $5\times5\times5$ nodes on the three bounding faces of the master domain $[-1,1]\times[-1,1]\times[-1,1]$. These shape functions are used to generate the P_{x_1}, P_{x_3} and P_t FE basis functions and used in Eq. (16). Thus, $A_{m_{iln}}^k$ equals the values of the $m(=7)$ solution variables at the ith, lth and mth node along the x_1-, x_3- and t-axes in the kth layer, respectively. For 5 nodes on an element along the t-axis, this technique simultaneously provides values of the $7P_{x_1}P_{x_3}$ unknowns in each layer at four times, since the solution at the first node in the time domain equals the initial values incorporated into the definition of J in Eq. (19). This process is repeated N_t times to compute the solution at the final time T.

Evaluating the integrals using nodes as integration points (Gauss–Lobatto rule of integration) in Eqs. (21) provide the $7\times P_{x_1}\times P_{x_3}\times P_t$ algebraic equations per layer. Assembling these equations yields the following global system of equations:

$$\begin{bmatrix} \mathbf{K}^{\sigma_{13}\sigma_{13}} & \mathbf{K}^{\sigma_{13}\sigma_{33}} & \mathbf{K}^{\sigma_{13}\epsilon_{11}} & \mathbf{K}^{\sigma_{13}v_1} & \mathbf{K}^{\sigma_{13}v_3} & \mathbf{K}^{\sigma_{13}u_1} & \mathbf{K}^{\sigma_{13}u_3} \\ & \mathbf{K}^{\sigma_{33}\sigma_{33}} & \mathbf{K}^{\sigma_{33}\epsilon_{11}} & \mathbf{K}^{\sigma_{33}v_1} & \mathbf{K}^{\sigma_{33}v_3} & \mathbf{K}^{\sigma_{33}u_1} & \mathbf{K}^{\sigma_{33}u_3} \\ & & \mathbf{K}^{\epsilon_{11}\epsilon_{11}} & \mathbf{K}^{\epsilon_{11}v_1} & \mathbf{K}^{\epsilon_{11}v_3} & \mathbf{K}^{\epsilon_{11}u_1} & \mathbf{K}^{\epsilon_{11}u_3} \\ & & & \mathbf{K}^{v_1v_1} & \mathbf{K}^{v_1v_3} & \mathbf{K}^{v_1u_1} & \mathbf{K}^{v_1u_3} \\ & & \mathbf{SYM.} & & \mathbf{K}^{v_3v_3} & \mathbf{K}^{v_3u_1} & \mathbf{K}^{v_3u_3} \\ & & & & & \mathbf{K}^{u_1u_1} & \mathbf{K}^{u_1u_3} \\ & & & & & & \mathbf{K}^{u_3u_3} \end{bmatrix} \times \begin{Bmatrix} \sigma_{13} \\ \sigma_{33} \\ \epsilon_{11} \\ \mathbf{v}_1 \\ \mathbf{v}_3 \\ \mathbf{u}_1 \\ \mathbf{u}_3 \end{Bmatrix} = \begin{Bmatrix} \mathbf{F}^{\sigma_{13}} \\ \mathbf{F}^{\sigma_{33}} \\ \mathbf{F}^{\epsilon_{11}} \\ \mathbf{F}^{v_1} \\ \mathbf{F}^{v_3} \\ \mathbf{F}^{u_1} \\ \mathbf{F}^{u_3} \end{Bmatrix}. \tag{23}$$

3.2. Time-marching procedure

For large values of T, the number of unknowns can become enormous. One way to overcome this is to solve the problem on the domain $D_i = [0, L]\times[-\frac{h}{2}, \frac{h}{2}]\times[t_{i-1}, t_i]$, $t_0 = 0$ where $[t_{i-1}, t_i]$ is the length of the element along the t-axis. Once the solution on D_1 has been computed, the solution at t_1 serves as the initial condition for the problem on D_2. This process is then repeated until the final time of interest. Because the integration algorithm is implicit, stability is not an issue. Accuracy of the solution, however, depends upon the time step size.

4. Numerical results and discussion

Effects of the beam aspect ratio (AR = L/h), facesheet-core thickness ratio (FCTR = h^c/h^f) and the in-plane and transverse facesheet-core stiffness ratio (FCISR, FCTSR) on the maximum centroidal deflection of the bottom facesheet, the Tsai–Wu failure index, and the FFL are elucidated. We first analyze two example problems and compare the present results to those computed with the commercial FE software

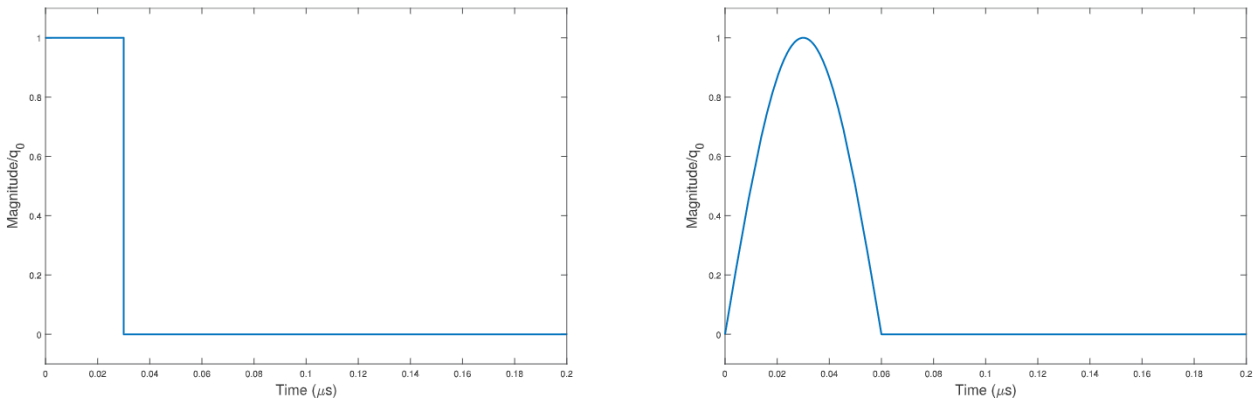

(a) Rectangular pulse (b) Sinusoidal pulse

Fig. 6. Time histories of the applied pressure pulse at $x_3 = 1.009$ mm.

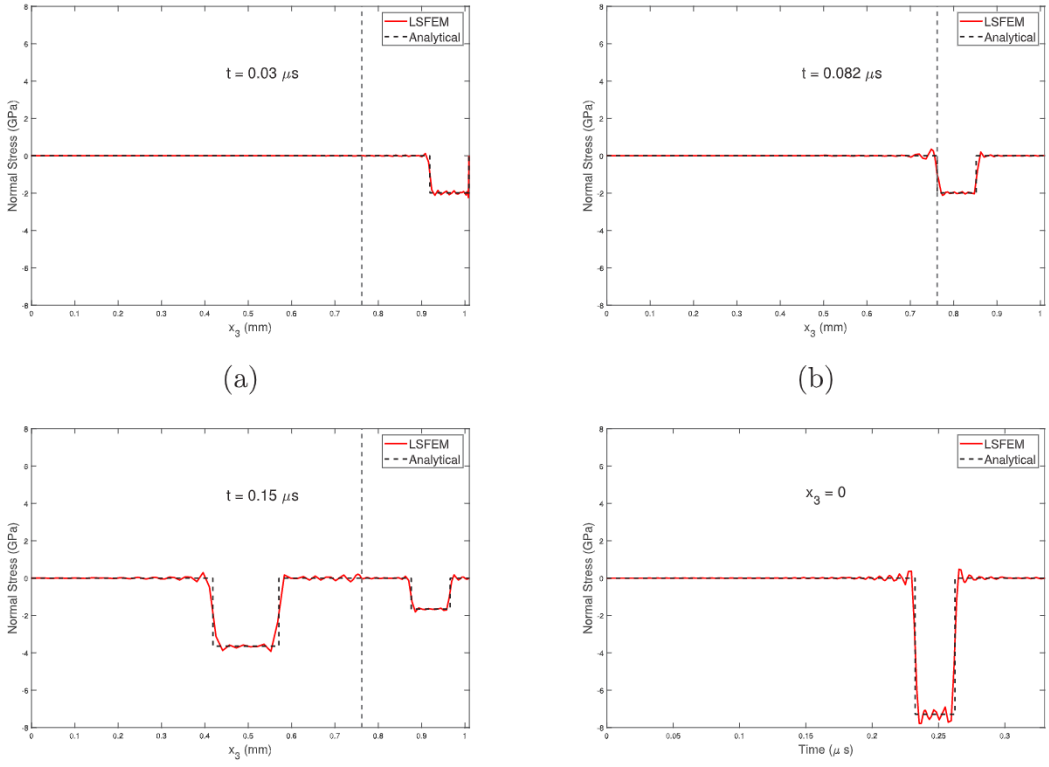

(a) (b) (c) (d)

Fig. 7. Comparison of 1-D wave propagation present results (indicated by LSFEM) with the analytical solution.

ABAQUS, and illustrate convergence with respect to the mesh parameters. Sensitivity studies are performed in Section 4.2 to statistically quantify the effect that the ratios have on the beam's maximum deflection and the FFL. In Sections 4.2 and 4.1.2, beam layers are assumed to be made from the same base material, with the following material properties:

$$E_{11} = 172.4\,\text{GPa}, \quad E_{22} = E_{11}/25, \quad E_{33} = E_{22},$$
$$G_{12} = G_{13} = 0.5E_{22}, \quad G_{23} = 0.2E_{22},$$
$$\nu_{12} = \nu_{13} = \nu_{23} = 0.25,$$
$$\rho = 1500\,\frac{\text{kg}}{\text{m}^3}, \quad X_T = 1.515\,\text{GPa}, \quad X_C = 1.697\,\text{GPa},$$
$$Z_T = 43.8\,\text{MPa}, \quad Z_C = 43.8\,\text{MPa}, \quad S = 86.9\,\text{MPa}.$$

In this case, "base material" refers to the case when each layer is made of a homogeneous material for $FCSR \neq 1$, the E_{11} property of the core is modified and the others are changed according to the relationships given above. It is assumed that the strength parameters X_T, X_C, Z_T and Z_C remain unaltered for the core material for different stiffness ratios. Sandwich beams with facesheet and core materials having different FCISR's and FCTSR's are studied in Section 4.3. A normal surface traction on the top surface of the beam of the form in Eq. (24) is assumed for the problems studied in Sections 4.1.2, 4.2 and 4.3 (see Fig. 4), where $q_0(x_1)$ is either constant or sinusoidal in space where noted. In these subsections, the length of the beam is held fixed at $L = 1$ m and the numerical solution is computed for $T = 1$ ms. For the bottom

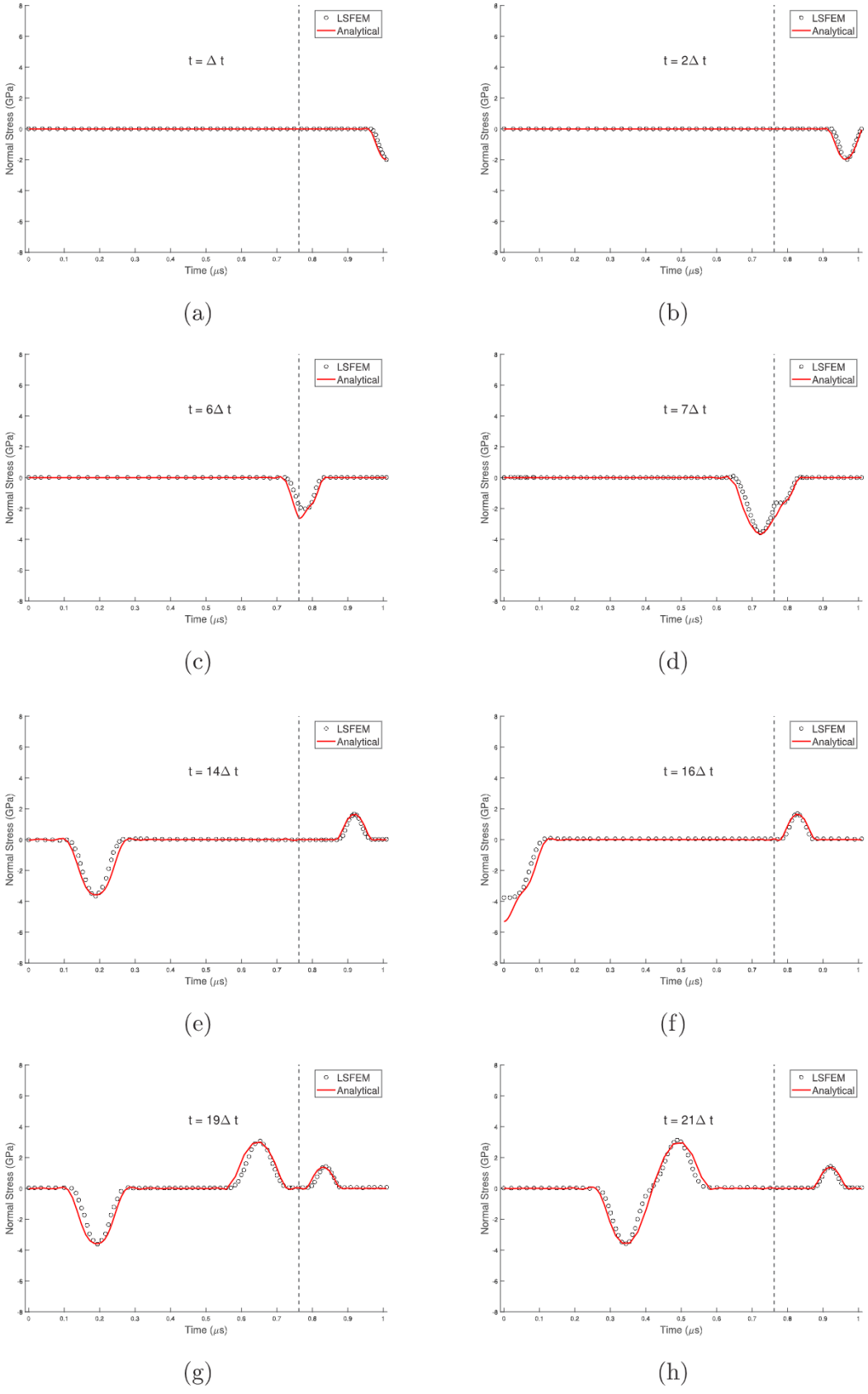

Fig. 8. Comparison of the present 1-D wave propagation results (indicated by LSFEM) with those from Ref. [27] at different time steps.

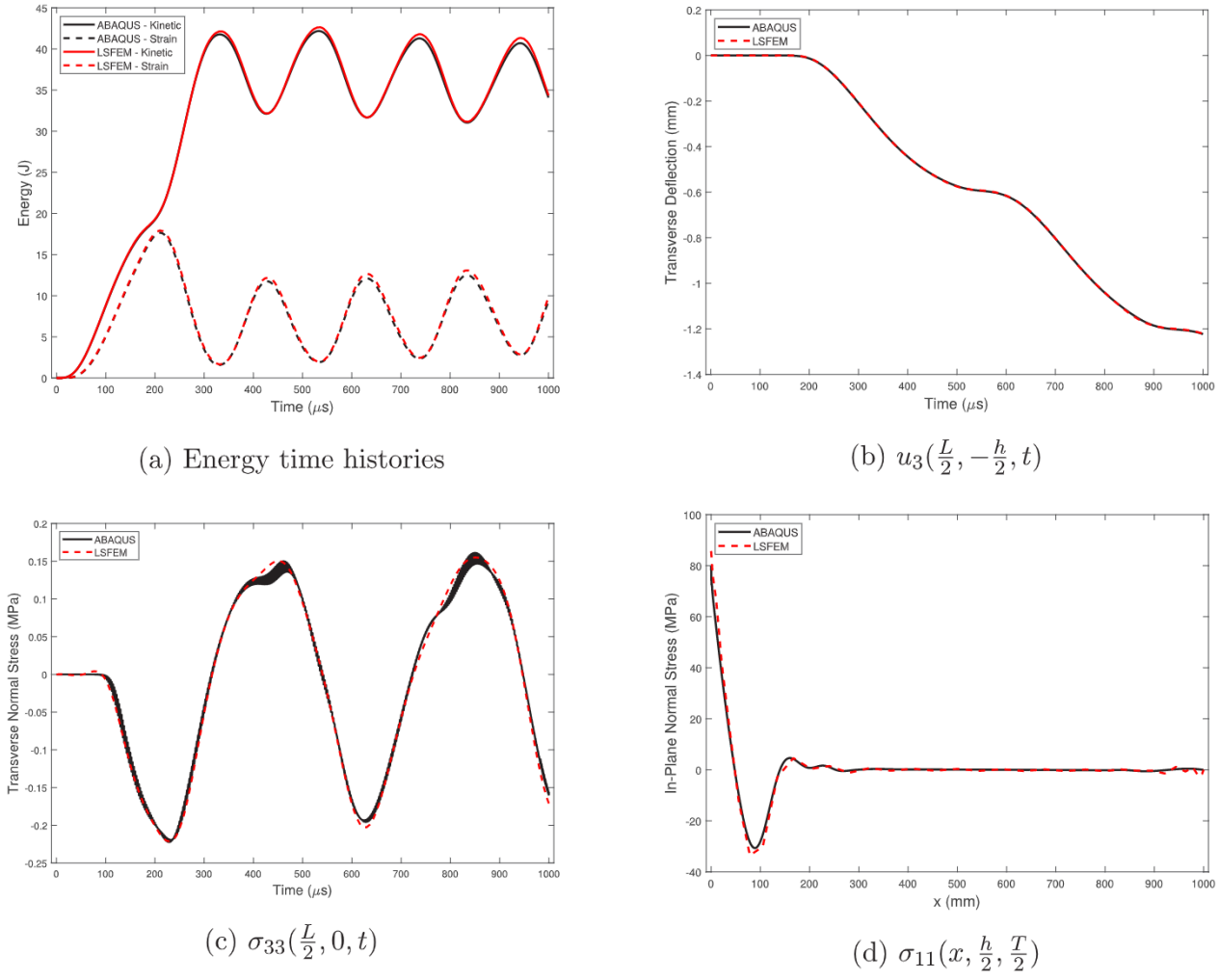

(a) Energy time histories

(b) $u_3(\frac{L}{2}, -\frac{h}{2}, t)$

(c) $\sigma_{33}(\frac{L}{2}, 0, t)$

(d) $\sigma_{11}(x, \frac{h}{2}, \frac{T}{2})$

Fig. 9. Comparison of the present results (indicated by LSFEM) with those from ABAQUS for Example 1.

surface, $q_0(x_1) = 0$.

$$P(x_1, t) = q_0(x_1) \sin\left(\frac{2\pi t}{T}\right) \exp\left(-\frac{10t}{T}\right). \tag{24}$$

4.1. Results for two example problems

4.1.1. Pressure pulse in a heterogeneous bar

In the first example problem, a 2-layer heterogeneous bar, shown in Fig. 5, is subjected to a uniform pressure on the top surface. This problem was also studied in Ref. [27]. We consider two different load time histories, shown in Fig. 6, which correspond to a rectangular and a sinusoidal pulse, respectively. Material properties for the two layers are provided in Table 1, with Poisson's ratio set to zero to compare results with those for wave propagation in a bar. Null velocities and displacements are enforced at $x_3 = 0$ and null tractions $(\sigma_{11}, \sigma_{13})$ at $x_1 = 0, L$.

We check if our formulation correctly predicts the wave speeds of the propagating pressure pulse in each layer and the transmission and reflection of the wave at layer interfaces and boundaries. We also seek to explore how p-refinement of the basis functions in x_3- and t-directions affects the solution's accuracy. However, we consider one element in the x_1-direction with quadratic polynomials (i.e., $P_{x_1} = 3$) since deformations are expected to be essentially uniform on a plane x_3 = constant. Results from the convergence study are shown in Table 2, where we compute the normal stress at the material interface at times $t = 5\Delta t$ and $t = 15\Delta t$, and $\Delta t = 0.03\,\mu$s is width of the rectangular pulse. For convergence, the solution for an initial mesh is computed, and then the polynomial degrees are increased in one direction at a time (for x_3 and t) until the relative percent change in σ_{33} falls below 1% from its value obtained with the immediately preceding mesh. Once this criterion is met for both polynomial degrees, the number of time steps is increased until the 1% threshold is met once again. The converged mesh from Table 2, including all three directions and seven nodal variables, contains 13,209 degrees of freedom per time step, and the analysis is run for $25\Delta t$, or 0.75 μs.

Table 1
Values of material parameters.

Material 1		Material 2	
E (GPa)	$\rho(\frac{g}{cm^3})$	E (GPa)	$\rho(\frac{g}{cm^3})$
10.788	1.2	203.92	7.896

The longitudinal (1-D) wave speed given by

$$c = \sqrt{\frac{E}{\rho}}, \tag{25}$$

for layers 1 and 2 equals 2,998 m/s and 5,082 m/s, respectively, for the material properties given in Table 1. The incident wave reaches the material interface at $t = 0.082\,\mu$s, at which time a portion of the wave is transmitted into material 2 while some of it is reflected back

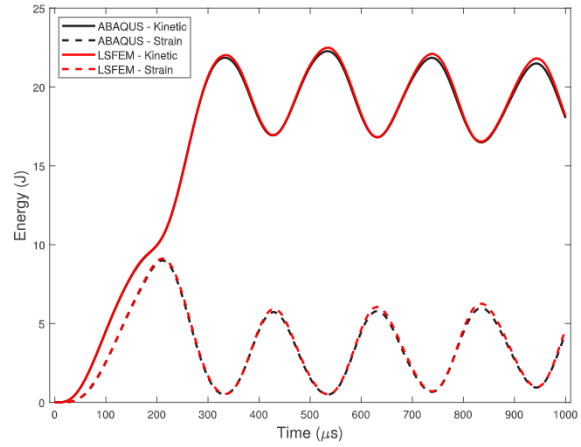

(a) Energy time histories

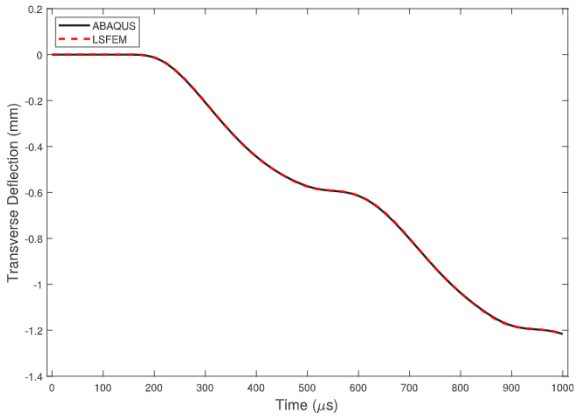

(b) $u_3(\frac{L}{2}, -\frac{h}{2}, t)$

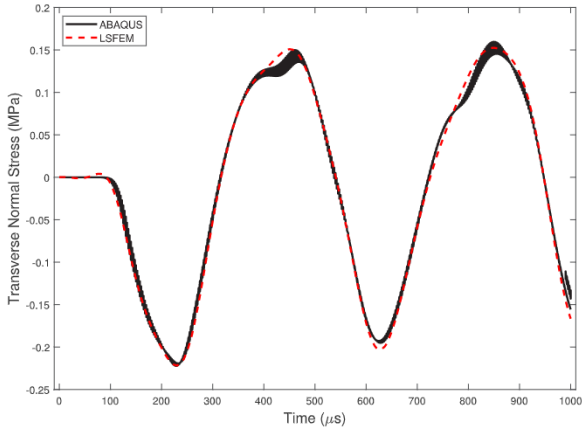

(c) $\sigma_{33}(\frac{L}{2}, 0, t)$

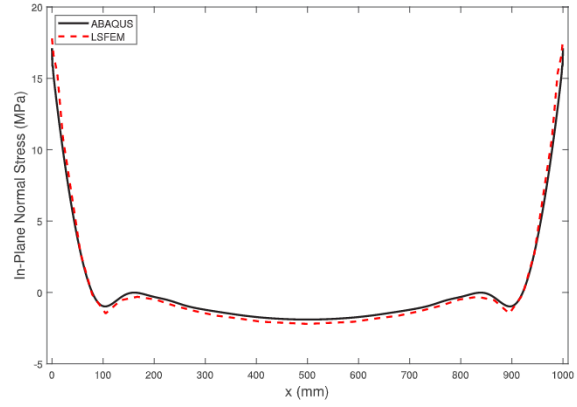

(d) $\sigma_{11}(x, \frac{h}{2}, \frac{T}{2})$

Fig. 10. Comparison of the present results (indicated by LSFEM) with those from ABAQUS for Example 2.

into material 1, governed by the following relations [36]:

$$\beta_T = \frac{2\rho_2 c_2}{\rho_2 c_2 + \rho_1 c_1} = 1.835$$
$$\beta_R = \frac{\rho_2 c_2 - \rho_1 c_1}{\rho_2 c_2 + \rho_1 c_1} = 0.835, \tag{26}$$

where β_T and β_R are the transmitted and the reflected coefficients, respectively. Applying Eq. (26) and using the material properties listed in Table 1, the theoretical transmitted and reflected stress wave amplitudes are 3.645 and 1.659 GPa, respectively. The wave should then arrive at the clamped edge ($x_3 = 0$) at time $t = 0.232$ μs, where the wave's amplitude should increase by a factor of two to 7.29 GPa. After this time, more interactions with transmitted and reflected waves occur.

For the load time history of Fig. 6(a) with $q_0 = 1.986$ GPa, Fig. 7(a)–(c) show the stress distribution through the length of the bar at $t = 0.03$, 0.082 and 0.15 μs. The time history of the normal stress at the clamped edge ($x_3 = 0$) is depicted in Fig. 7(d). Note that the compressive wave travels to the left from $x_3 = 1.009$ to $x_3 = 0$. The front edge of the wave should arrive at the interface $x_3 = 0.762$ mm in $0.247/2.998 = 0.82$ μs that is close to the computed time of arrival of the wave front. We note that the wave front has been distorted somewhat and we see the Gibbs phenomenon that is often present when the ordinary differential equations in time are integrated using the finite-difference method.

Upon reaching the interface $x_3 = 0.762$ mm, Eq. (26) provides fractions of the wave transmitted into layer 2 and reflected back into layer 1. The theoretical transmitted and reflected stress wave amplitudes are 3.645 and 1.659 GPa, respectively. Since the acoustic impedance of material 2 is about 8.5 times that of material 1, a compressive wave is reflected back as a compressive wave. The transmitted wave should then arrive at the clamped edge ($x_3 = 0$) at time $t = 0.232$ μs, where the wave's amplitude should increase by a factor of two to 7.29 GPa. The computed results exhibited in Fig. 7(c),(d) are very close to their analytical counterparts.

For the load time history of Fig. 6(b), Fig. 8(a)–(h) evince the stress distribution through the length of the bar at different times. The computed results compare favorably with those digitized from plots of Ref. [27], which were computed using a four element uniform

Table 2
Convergence of the presently computed results for the pressure pulse of Fig. 6(a) with $P_{x_3} = 3$, $N_t = 20$ ($N_t = 40$ for the final row) and increasing degree of polynomials in the x_3 and time directions. Values of σ^1_{33} and σ^2_{33}, respectively, equal the axial stress at the interface $x_3 = 0.762$ mm at $t = 0.15$ and 0.45 μs.

P_{x_3}	P_t	σ^1_{33}	% Diff.	σ^2_{33}	% Diff.
10	4	−0.1386	–	−0.5338	–
14	4	−0.1323	4.545	−0.5420	1.536
18	4	−0.1323	0.020	−0.5419	0.013
18	6	0.0628	147.510	−0.0608	88.77
18	8	−0.0374	159.525	0.2878	572.9
18	10	0.0166	144.264	0.3309	15.01
18	12	0.0083	49.954	0.3336	0.798
18	14	0.0051	37.805	0.3361	0.760
18	16	0.0052	0.4915	0.3375	0.422
18	16	0.0051	0.9538	0.3359	0.486

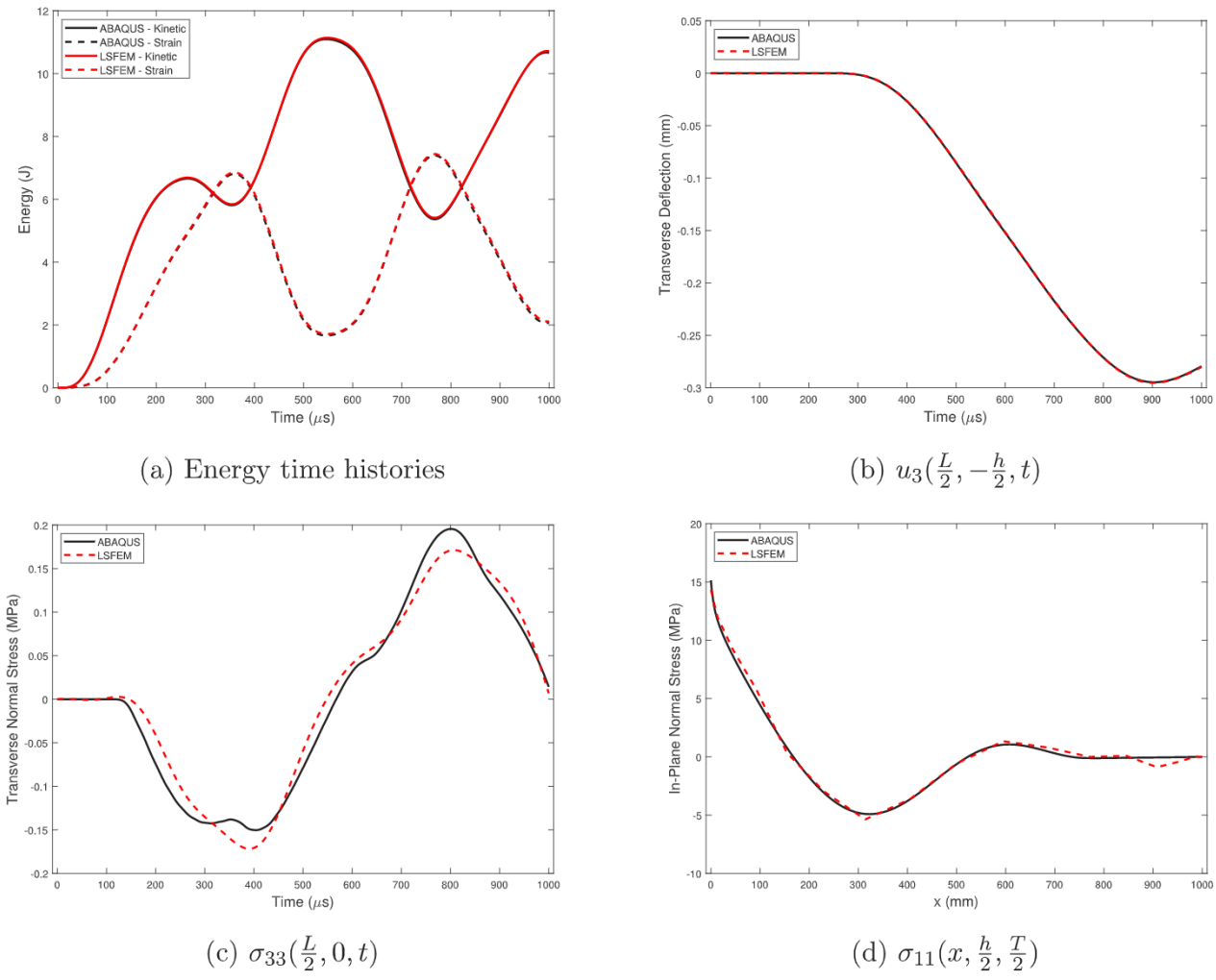

(a) Energy time histories

(b) $u_3(\frac{L}{2}, -\frac{h}{2}, t)$

(c) $\sigma_{33}(\frac{L}{2}, 0, t)$

(d) $\sigma_{11}(x, \frac{h}{2}, \frac{T}{2})$

Fig. 11. Comparison of the present results (indicated by LSFEM) with those from ABAQUS for Example 3.

discretization for space–time strip and 9th degree polynomials in each direction, with a couple of notable exceptions. The pressure wave traveling from right to left should arrive at the material interface just before the $6\,\Delta t$ time interval. From Fig. 8(c), the predicted wave in [27] just arrives at the interface at $t = 6\,\Delta t$, which indicates that their calculated wave speed is off slightly. Our work, however, predicts that the wave has just begun being transmitted and reflected at this time, as it should. This also explains the discrepancy in the waveform in Fig. 8(d), in addition to the time history of the pulse being approximated by a sinusoidal input. Predictions from the two works also differ at the clamped edge, where [27] predicts the wave maintaining its amplitude when it arrives at the boundary, which disagrees with the analytical value of 7.29 GPa.

4.1.2. Transient deformations in four sandwich beams

We now consider four sandwich beams with different design parameters, boundary conditions and loading, and compare solutions to those obtained using ABAQUS. The surface traction magnitude q_0 in Eq. (24) is set equal to 1 MPa and values of other parameters are given in Table 3, where a sinusoidal load indicates a non-uniform spatial distribution on the top surface in Eq. (24) of the form $q_0 = \sin\frac{\pi x_1}{L}$. Clamped and free boundary conditions are indicated with "CC" and "FF", respectively.

We explore convergence of the numerical solution for Examples 2 and 4 by considering only a single element in the x_1-direction, which is a similar strategy to that employed in [37] where a Ritz method was used to obtain accurate results for static stresses and natural frequencies. The same convergence criterion as in the previous section is used and we compute the transverse deflection u_3 at $x_1 = \frac{L}{2}$, $x_3 = -\frac{h}{2}$, $t = \frac{T}{2}$ and in-plane normal stress at $x_1 = 0.05L$, $x_3 = \frac{h}{2}$, $t = \frac{T}{2}$, shown in Tables 4 and 5. The converged solutions are for 19,600 and 9,520 degrees of freedom for Examples 2 and 4, respectively. We compare these solutions to those obtained with ABAQUS using CPS4R bilinear quadrilateral plane stress elements with reduced integration and an explicit time integration scheme, where a similar convergence criteria is used as with the LSFEM solutions. Results in Tables 4 and 5 imply that the deflection converges rather quickly even with a low degree of polynomials in the x_1 direction for a thick beam, but a much higher degree of polynomials is needed for a thin beam. As mentioned in [37], it is due to several modes participating in the beam deformation when it is thin and fewer when it is thick. We did not study the error, if any, introduced by using the reduced integration in ABAQUS.

Figs. 9–12 show the comparison of selected results between the LSFEM formulation and ABAQUS. Time histories of the kinetic and

Table 3
Parameters and data for the four example problems.

Example	AR	FCTR	FCSR	B.C.	Load
1	50	5	500	CC–FF	Uniform
2	50	5	500	CC–CC	Sinusoidal
3	10	2	100	CC–FF	Uniform
4	10	2	100	CC–CC	Sinusoidal

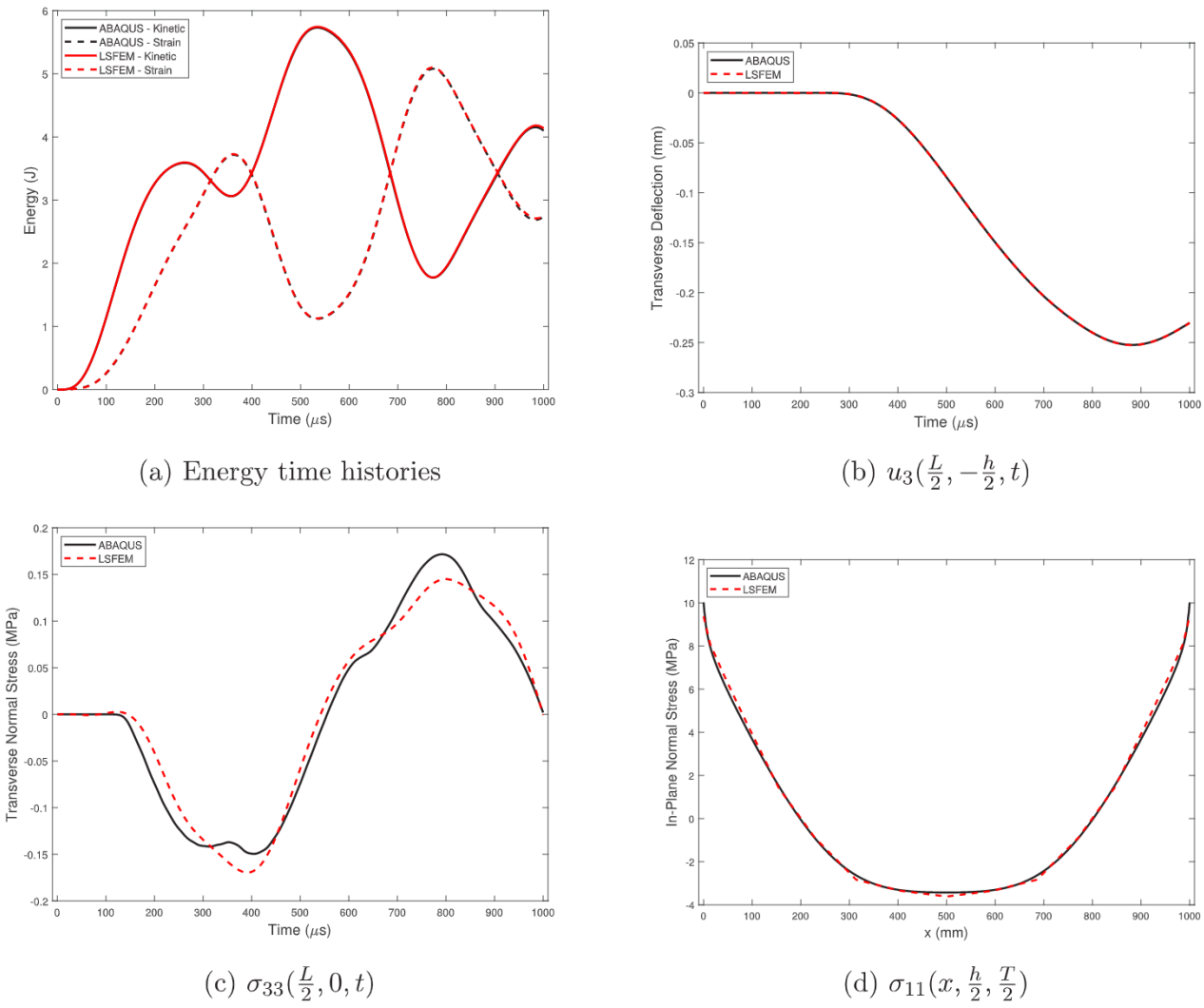

(a) Energy time histories

(b) $u_3(\frac{L}{2}, -\frac{h}{2}, t)$

(c) $\sigma_{33}(\frac{L}{2}, 0, t)$

(d) $\sigma_{11}(x, \frac{h}{2}, \frac{T}{2})$

Fig. 12. Comparison of the present results (indicated by LSFEM) with those from ABAQUS for Example 4.

Table 4
LSFEM convergence results for Example 2.

P_{x_1}	P_{x_3}	P_t	N_{x_1}	N_t	u_3 (mm)	% Diff.	σ_{11} (MPa)	% Diff.
10	3	3	1	20	−0.5037	–	50199	–
16	3	3	1	20	−0.5019	0.3681	3.512	32.4419
22	3	3	1	20	−0.5016	0.0483	3.986	13.5002
28	3	3	1	20	−0.5016	0.0083	3.901	2.1409
34	3	3	1	20	−0.5016	0.0060	3.948	1.2156
34	4	3	1	20	−0.5058	0.8355	4.112	4.1494
34	5	3	1	20	−0.5032	0.5061	4.087	0.6174
34	5	4	1	20	−0.5034	0.0402	4.092	0.1151
34	5	4	1	40	−0.5032	0.0449	4.091	0.200

Table 5
LSFEM convergence results for Example 4.

P_{x_1}	P_{x_3}	P_t	N_{x_1}	N_t	u_3 (mm)	% Diff.	σ_{11} (MPa)	% Diff.
10	3	3	1	20	−0.1309	–	6.240	–
16	3	3	1	20	−0.1308	0.0764	6.226	0.2286
16	4	3	1	20	−0.1316	0.6116	6.069	2.5139
16	5	3	1	20	−0.1315	0.0760	6.127	0.9488
16	5	4	1	20	−0.1315	0.0139	6.135	0.1288
16	5	4	1	40	−0.1315	0.0269	6.095	0.6451

strain energies are in good agreement for all four examples, with a maximum difference of 5% between the two solutions occurring at around time $t = 950\,\mu$s for the kinetic energy. The transverse deflections of the bottom facesheet mid span are also in excellent agreement. For the two thin sandwich beams (Examples 1 and 2), the transverse normal stress time history of the beam's centroid match very well overall, with the LSFEM solution predicting a 13% higher peak stress around time $t = 842\,\mu$s. In the two thicker beams, the two centroidal transverse stress histories are in excellent agreement. The spatial variation of the in-plane normal stress σ_{11} at the top of the beam at $t = \frac{T}{2}$ also match well, though the LSFEM solution has slight oscillations near the free edge. These can be alleviated by increasing the polynomial order in the x_1-direction at the expense of more degrees of freedom, though this was not pursued here. The in-plane normal stress σ_{11} at a clamped edge computed from the two software differs at most by 7.23%, 4.03%, 5.47% and 6.41% for the four examples. Note that σ_{11} is not a nodal variable. The displacement-based FEM provides accurate values of the nodal displacements but stresses derived from them deviate somewhat from their analytical values.

Most commercial software, including ABAQUS, use a displacement-based formulation and an explicit time integration scheme for analyzing linear elasto-dynamic problems. With the refinement of the FE mesh and a decrease in the time-step size they provide accurate values of the displacements. However, finding stresses and satisfying continuity conditions at interfaces between two adjoining layers of extreme stiffness ratios is very challenging; e.g., see [37] where it is shown that the 6th frequency fails to converge to the analytical value with the mesh refinement. The present work based on the state-space formulation uses

Table 6
Sensitivity results.

	Deflection		Tsai–Wu Index		FFL	
Source	f-statistic	p-value	f-statistic	p-value	f-statistic	p-value
AR	809	0	85	0	72	0
FCTR	0.01	0.9193	3	0.0815	36	0
FCISR	0.17	0.6824	1	0.2489	0.5	0.4684
AR*FCTR	0.14	0.7055	594	0	18	0
AR*FCISR	0.71	0.4004	8	0.0054	0	0.9722
FCTR*FCISR	0.18	0.6701	70	0	0.2	0.6873

both stresses and displacements as nodal unknowns and provides their accurate values. However, the computed value of the stress component not included as a nodal variable differs from its analytical value by about 10%. As mentioned before we have not explored if further refinement of the FE mesh will reduce this difference.

4.2. Sensitivity analysis for a clamped beam

To study how sensitive the maximum deflection, the Tsai–Wu failure index and the FFL (q_0) are to the different ratios discussed previously, we use the Latin Hypercube Sampling method (LHS) to generate 300 designs for clamped–clamped beams with ranges of [2,100], [1,20] and [1,2500] for the AR, FCTR and FCISR, respectively. Results from the generated designs are used to perform an analysis of variance (ANOVA) in MATLAB for each of the three quantities and determine which factors play a significant role. We calculate the f-statistic and the p-value, which measure the ratio of the variation in sample means to the variation within the samples and the probability of observing an f-statistic greater than or equal to the value obtained, respectively. Factors for which the p-values which are closer to one play little to no role in the observed behavior, while those for the which the p-values are close to zero indicate much higher significance; the opposite relationship is true for the f-statistic. The three inputs (AR, FCTR, FCSR) and their interactions (AR*FCTR, AR*FCISR, FCTR*FCISR) are used as predictors in the analysis.

The magnitude of the load $q_0(x_1)$ in Eq. (24) is assumed to be uniform and set to one megapascal (MPa) for studying sensitivities of the maximum deflection and the Tsai–Wu index, while the magnitude is varied for the FFL case until the maximum Tsai–Wu index reaches around 0.98 (or very close to failure). To determine the maximum Tsai–Wu index, its value is calculated at each spatial node for every temporal node in the mesh and the overall maximum value is taken. We also note that the location of the maximum Tsai–Wu failure index for each case studied occurred at a clamped boundary in the top facesheet. A mesh of $P_{x_1} = 40$, $P_{x_3} = 5$, $P_t = 5$, $N_{x_1} = 1$, $N_t = 40$ is used for each beam design in the analysis due to the higher degree polynomials needed for beams with higher FCSRs, as shown by Example 2 in Section 4.1.2.

ANOVA results for the three quantities are summarized in Table 6. The maximum deflection is overwhelmingly sensitive to the AR, with an f-statistic of 809 and p-value of zero, and very insensitive to all of the other ratios. While the maximum Tsai–Wu index is also very sensitive to the AR ($f_{AR} = 85$), it is far more sensitive to the interaction between the AR and FCTR, indicated by $f_{AR/FCTR} = 594$ and a p-value of 0. There is also a sensitivity to the FCTR–FCISR interaction, though to a lesser extent than that to the AR. Finally, the FFL is mostly sensitive to the AR, FCTR and their interaction with virtually no sensitivity to the FCISR.

4.3. Failure analysis with different facesheet and core materials

We now consider sandwich beams with facesheet and core materials that have different stiffness ratios in the 1- and 3-directions. Properties for the facesheets and the core materials are provided in Table 7 in GPa and strength values are given in Table 8 in MPa. Each facesheet in Tables 7–8 is paired with the two core materials, and the maximum facesheet deflection, the Tsai–Wu failure index and FFL are computed for the nine facesheet/core combinations and AR = 10, 50 and 100. Results are listed in Table 9(a)–(c). The same mesh as in Section 4.2 is used here.

Table 7
Facesheet and core material properties, moduli are in GPa, the mass density is in kg/m^3.

Facesheet:	E_{11}	E_{22}	E_{33}	G_{12}	G_{13}	G_{23}	ν_{12}	ν_{13}	ν_{23}	ρ
Graphite/Epoxy 1	132.5	10.8	10.8	5.7	5.7	3.4	0.24	0.24	0.30	1540
Glass/Epoxy 2	49.3	14.7	14.7	6.8	6.8	4.9	0.30	0.31	0.49	2000
Aramid/Epoxy 3	17.2	17.2	10.3	5.5	3.3	3.3	0.20	0.12	0.12	1117
Core:										
Balsa	0.5	0.5	21.9	0.08	0.60	0.57	0.50	0.01	0.01	495
Foam H45	0.05	0.05	0.05	0.01	0.01	0.01	0.40	0.40	0.40	48

Table 8
Facesheet and core strengths (MPa).

Facesheet:	X_T	X_C	Z_T	Z_C	S
Graphite/Epoxy 1	1515	1697	48.3	48.3	86.9
Glass/Epoxy 2	1675	1220	48.3	210.9	108.0
Aramid/Epoxy 3	425	88	255	53	40
Core:					
Balsa	2.7	2.8	54.4	73.8	6.4
Foam H45	1.1	0.5	1.1	0.5	0.46

Similar to the previous section, the AR has a significant impact on the maximum deflection, the Tsai–Wu index and the FFL when the stiffness ratios in the two materials differ. In the graphite/balsa case, increasing the AR dramatically increases (decreases) the maximum deflection and the Tsai–Wu index (FFL), while increasing the FCTR has a similar yet much smaller effect. For example, increasing the AR from 10 to 100 ($FCTR = 2$) decreases the FFL by 77%, and by 19% when increasing the FCTR from 2 to 20 ($AR = 10$). It can also be seen from Table 9 that changing the FCTR has much less effect on the failure index and FFL as the AR increases. When the foam core is used, which has a much higher FCTSR than the balsa core, the maximum deflection and the Tsai–Wu index (FFL) increases (decreases) dramatically. In this case, increasing the FCTR has much less effect when the AR is lower, which is opposite that of the balsa core. Nearly identical observations hold for the glass and aramid epoxy facesheets. In general, the glass facesheets have the highest FFLs while the aramid facesheets have the lowest. In addition, there are several instances of the beam surpassing a failure index of one when the foam core is used, for all facesheets considered. These observations demonstrate the pronounced effect that the FCTSR has on the dynamic behavior and failure of composite sandwich beams.

We note that authors of Refs. [38] and [39] have used a third order shear and normal deformable plate/shell theory, the Tsai-Wu failure criteria and the progressive failure analysis to ascertain the first failure and the ultimate failure loads of sandwich structures.

5. Conclusions

Plane stress infinitesimal elastodynamic deformations and the first failure loads of sandwich composite beams have been studied by first writing the governing equations in the state-space form. Each variable is expressed in terms of the Gauss–Lobatto–Legendre polynomials as basis functions. The sum of the squares of the residuals of these equations and of the initial and boundary conditions integrated over the space and time domains is minimized to derive the system of simultaneous linear algebraic equations. The computed results for several problems have been compared with available either analytical or published

Table 9
Results for different facesheet/core material beams. The maximum back facesheet deflection (u_3) is in mm, and FFL ($q_{0_{max}}$) in MPa. The stiffness ratios E^f_{11}/E^c_{11} and E^f_{33}/E^c_{33} are also listed. We note that for the maximum deflections and Tsai–Wu failure indices (column 1 and 2), the uniform applied load $q_0 = 1$ MPa. For the FFL (column 3), q_0 is increased until the maximum Tsai–Wu failure index in the beam is close to 1.0 (i.e. $F_{max} \approx 0.98$). Note that $q_{0_{max}}$ approximately equals $1/\sqrt{F_{max}}$ further verifying the accuracy of the work since the expression for F is quadratic in stress components with respect to the material principal axes.

Core material	FCTR	AR = 10			AR = 50			AR = 100		
		u_3	F_{max}	$q_{0_{max}}$	u_3	F_{max}	$q_{0_{max}}$	u_3	F_{max}	$q_{0_{max}}$
(a) Graphite/epoxy 1 facesheets.										
Balsa	2	0.22	$5.9E^{-3}$	13.04	2.24	$4.6E^{-2}$	4.65	4.60	0.11	2.99
$E^f_{11}/E^c_{11} = 265$	5	0.29	$6.2E^{-3}$	12.82	2.89	$4.5E^{-2}$	4.75	5.86	0.11	3.03
$E^f_{33}/E^c_{33} = 0.49$	10	0.34	$7.6E^{-3}$	11.75	3.55	$4.5E^{-2}$	4.78	6.63	0.11	3.00
	20	0.39	$1.0E^{-2}$	10.48	4.19	$5.0E^{-2}$	4.63	6.74	0.12	2.90
Foam H45	2	0.51	0.28	2.82	2.24	0.44	1.55	4.89	1.87	0.73
$E^f_{11}/E^c_{11} = 2409$	5	0.94	0.33	2.33	4.19	0.83	1.09	8.20	3.17	0.55
$E^f_{33}/E^c_{33} = 196.4$	10	1.48	0.36	2.18	6.51	1.36	0.85	13.12	4.88	0.45
	20	2.08	0.38	2.04	10.64	2.08	0.68	21.35	7.35	0.36
(b) Glass/epoxy 2 facesheets.										
Balsa	2	0.23	$6.3E^{-3}$	14.70	1.91	$2.8E^{-2}$	5.95	2.82	$6.9E^{-2}$	3.83
$E^f_{11}/E^c_{11} = 98.6$	5	0.31	$7.9E^{-3}$	14.73	2.59	$3.2E^{-2}$	5.71	3.79	$8.0E^{-2}$	3.59
$E^f_{33}/E^c_{33} = 0.67$	10	0.38	$9.1E^{-3}$	14.66	3.15	$4.0E^{-2}$	5.18	4.69	0.11	3.11
	20	0.46	$8.4E^{-3}$	12.80	3.47	$6.2E^{-2}$	4.19	5.77	0.22	2.14
Foam H45	2	0.50	0.27	2.65	1.90	0.48	1.52	3.76	1.54	0.80
$E^f_{11}/E^c_{11} = 896.4$	5	0.62	0.28	2.87	3.21	0.74	1.18	6.38	2.51	0.62
$E^f_{33}/E^c_{33} = 267.3$	10	0.88	0.34	2.27	5.20	1.10	0.94	10.37	3.75	0.51
	20	1.82	0.39	2.04	8.66	1.65	0.77	17.20	5.48	0.41
(c) Aramid/epoxy 3 facesheets.										
Balsa	2	0.37	$8.6E^{-2}$	9.25	2.66	0.26	3.26	4.60	0.49	1.83
$E^f_{11}/E^c_{11} = 34.5$	5	0.45	0.10	7.93	3.08	0.33	2.60	5.66	0.63	1.46
$E^f_{33}/E^c_{33} = 0.47$	10	0.54	0.12	6.98	3.20	0.40	2.19	6.66	0.77	1.22
	20	0.66	0.11	7.28	3.19	0.48	1.84	7.18	0.99	1.00
Foam H45	2	0.77	0.36	2.25	3.28	0.78	1.14	6.64	2.55	0.62
$E^f_{11}/E^c_{11} = 313$	5	1.03	0.34	2.29	5.50	1.14	0.92	10.94	3.86	0.49
$E^f_{33}/E^c_{33} = 188$	10	1.78	0.37	2.06	8.62	1.64	0.77	17.09	5.28	0.43
	20	2.58	0.45	1.86	13.50	2.28	0.54	26.53	6.95	0.29

solutions or those computed using the software ABAQUS. The Tsai–Wu criterion was used to identify failure initiation in sandwich beams and investigate the sensitivity of results to beam's aspect ratio (AR), facesheet-core thickness ratio (FCTR), facesheet-core in-plane stiffness ratio (FCISR, $\frac{E^f_{11}}{E^c_{11}}$) and facesheet-core transverse stiffness ratio (FCISR, $\frac{E^f_{33}}{E^c_{33}}$).

The main conclusions of this work are:

1. For the 1-D wave propagation in a bi-material bar subjected to two different pressure pulses, the computed wave propagation speeds and reflection/transmission of the incident wave at the material interface are in good agreement with their theoretical values. For a rectangular pulse, Gibbs phenomenon was observed.
2. For various problems studied, the computed quantities matched well with those obtained by using ABAQUS (CPS4R plane stress reduced integration elements), with a maximum of 13% difference in the transverse normal stresses in the core for thin beams, and a maximum of 7% deviation in the in-plane normal stress σ_{11} at clamped boundaries. In general, the two sets of results were very close to each other for thick beams.
3. An analysis of variance (ANOVA) showed that for clamped–clamped beams the aspect ratio (AR) dramatically affects the maximum back facesheet deflection, the Tsai–Wu failure index and the FFL. The Tsai–Wu failure index is very sensitive to the AR and the FCTR as well as to the inter-action between them. In the range of facesheet-core stiffness ratios (FCISR) considered ([1,2500]), the FCISR has little effect on these quantities.
4. Sandwich beams composed of three different facesheets (graphite/epoxy, glass/epoxy and aramid/epoxy) and two cores (balsa and foam H45) were considered. For the graphite/balsa case, in which the transverse stiffness ratio is small ($\frac{E^f_{33}}{E^c_{33}} = 0.49$), increasing the AR from 10 to 100 dramatically decreases the FFL and increases the maximum deflection. Increasing the FCTR from 2 to 20 has a similar but less pronounced effect. The FFL drops precipitously when the foam core is used ($\frac{E^f_{33}}{E^c_{33}} = 196.4$). Similar conclusions hold for the glass and aramid facesheets, with the glass (aramid) having higher (lower) FFLs.

Declaration of competing interest

The authors declare that they have no known competing financial interests or personal relationships that could have appeared to influence the work reported in this paper.

Acknowledgments

The financial support of the work from the U.S. Office of Naval Research (ONR) through grants N00014-18-1-2548, N00014-21-1-2283and N00014-20-1-2876 with Y. D. S. Rajapakse and Paul E. Hess as the Program Managers, to Virginia Polytechnic Institute and State University (Virginia Tech) with RCB as the PI is gratefully acknowledged. Views expressed in the paper are those of the authors and neither of the funding agency nor of Virginia Tech. We are grateful to Tim Tomlin of our Department for his help and guidance in using the computer cluster that was partially funded by an ONR Defense University Research Instrumentation Program (DURIP) grant.

Appendix A. Mixed plane stress elasticity constants

We provide here definitions of the mixed plane stress elasticity constants introduced in Section 2.1. These constants are obtained by setting out-of-plane stresses $\sigma_{22} = \sigma_{23} = \sigma_{12} = 0$ and expressing all out-of-plane and layer-wise discontinuous quantities in terms of ϵ_{11}, σ_{13}, and σ_{33}.

$$\hat{C}^k_{11} = \overline{C}^k_{11} - \frac{\overline{C}^{k^2}_{12}}{\overline{C}^k_{22}} + \frac{\overline{C}^k_{12}\overline{C}^k_{23}\hat{C}^k_{23}}{\overline{C}^k_{22}\hat{C}^k_{12}} - \frac{\overline{C}^k_{13}\hat{C}^k_{23}}{\hat{C}^k_{12}} \tag{A.1}$$

$$\hat{C}^k_{13} = \overline{C}^k_{13}\hat{C}^k_{23} - \frac{\overline{C}^k_{23}\overline{C}^k_{12}\hat{C}^k_{23}}{\overline{C}^k_{22}} \tag{A.2}$$

$$\hat{C}^k_{31} = \frac{\hat{C}^k_{13}}{\hat{C}^k_{23}} \tag{A.3}$$

$$\hat{C}^k_{33} = \overline{C}^k_{33} - \frac{\overline{C}^{k^2}_{23}}{\overline{C}^k_{22}} \tag{A.4}$$

$$\hat{C}^k_{44} = \overline{C}^k_{55} - \frac{\overline{C}^{k^2}_{45}}{\overline{C}^k_{44}} \tag{A.5}$$

$$\hat{C}_{12}^k = \frac{1}{\left(\overline{C}_{13}^k - \frac{\overline{C}_{12}^k \overline{C}_{23}^k}{\overline{C}_{22}^k}\right)} \tag{A.6}$$

$$\hat{C}_{23}^k = \frac{1}{\left(\overline{C}_{33}^k - \frac{\overline{C}_{23}^{k2}}{\overline{C}_{22}^k}\right)} \tag{A.7}$$

Appendix B. Elasticity constants for a transversely isotropic material

We provide here the components of the elasticity tensor, $\boldsymbol{C}$, for a transversely isotropic material in terms of engineering constants defined with respect to the material principal axes. In these definitions, the axis of transverse isotropy is along the x_1 direction and $E_{22} = E_{33}$.

$$\overline{C}_{11} = \frac{1 - \nu_{23}\nu_{32}}{E_{22}E_{33}\Delta} \tag{B.1}$$

$$\overline{C}_{12} = \frac{\nu_{21} + \nu_{23}\nu_{31}}{E_{22}E_{33}\Delta} \tag{B.2}$$

$$\overline{C}_{13} = \frac{\nu_{31} + \nu_{21}\nu_{32}}{E_{22}E_{33}\Delta} \tag{B.3}$$

$$\overline{C}_{22} = \frac{1 - \nu_{13}\nu_{31}}{E_{11}E_{33}\Delta} \tag{B.4}$$

$$\overline{C}_{23} = \frac{\nu_{32} + \nu_{12}\nu_{31}}{E_{11}E_{33}\Delta} \tag{B.5}$$

$$\overline{C}_{33} = \frac{1 - \nu_{12}\nu_{21}}{E_{11}E_{22}\Delta} \tag{B.6}$$

$$\overline{C}_{44} = G_{23} \tag{B.7}$$

$$\overline{C}_{55} = G_{13} \tag{B.8}$$

$$\overline{C}_{66} = G_{12} \tag{B.9}$$

$$\Delta = \frac{1 - \nu_{12}\nu_{21} - \nu_{23}\nu_{32} - \nu_{13}\nu_{31} - 2\nu_{21}\nu_{32}\nu_{13}}{E_{11}E_{22}E_{33}} \tag{B.10}$$

References

[1] L.J. Gibson, M.F. Ashby, Cellular Solids: Structure and Properties, Cambridge University Press, Cambridge, UK, 1999.

[2] P. Wanchoo, H. Matos, C.-E. Rousseau, A. Shukla, Investigations on air and underwater blast mitigation in polymeric composite structures- A review, Compos. Struct. (2020).

[3] D. Burns, R. Batra, Static deformations of fiber-reinforced composite laminates by the least-squares method, in: Modern Trends in Structural and Solid Mechanics 1: Statics and Stability, ISTE-Wiley, 2021, pp. 1–16.

[4] B.F. Vlasov, On one case of bending of rectangular thick plates, in: In Vestnik Moskovskogo Universiteta. Serieila Matematiki, Mekhaniki, Astronomii, Fiziki, Khimii, vol. 2, 1957, pp. 25–34.

[5] N.J. Pagano, Exact solutions for composite laminates in cylindrical bending, J. Compos. Struct. 3 (1969) 398–411.

[6] S. Srinivas, A.K. Rao, Bending, vibration and buckling of simply supported thick orthotropic rectangular plates and laminates, Int. J. Solids Struct. 6 (1970) 1463–1481.

[7] S.S. Vel, R.C. Batra, Analytical solutions for rectangular thick laminated plates subjected to arbitrary boundary conditions, AIAA J. 37 (1999) 1464–1473.

[8] S.S. Vel, R.C. Batra, The generalized plane strain deformations of thick anisotropic composite laminated plates, Int. J. Solids Struct. 37 (2000) 715–733.

[9] R.A. Toupin, Saint-Venant's principle, Arch. Ration. Mech. Anal. 18 (1965) 83–96.

[10] C.O. Horgan, Saint-Venant end effects in composites, J. Compos. Mater. 16 (1982) 411–422.

[11] L. Demasi, Quasi 2D and 3D exact solutions for bending of thick and thin sandwich plates, J. Sandw. Struct. Mater. 10 (2008) 271–310.

[12] L.Y. Bahar, A state space approach to elasticity, J. Franklin Inst. B 299 (1975) 33–41.

[13] T. Kant, C.K. Ramesh, Numerical integration of linear boundary value problems in solid mechanics by segmentation method, Int. J. Numer. Methods Eng. 17 (1981) 1233–1256.

[14] A.A. Khdeir, J.N. Reddy, Exact solutions for the transient response of symmetric cross-ply laminates using a higher-order plate theory, Compos. Sci. Technol. 34 (1989) 205–224.

[15] O. Song, J.S. Ju, L. Librescu, Dynamic response of anisotropic thin-walled beams to blast and harmonically oscillating loads, Int. J. Impact Eng. 21 (1998) 663–682.

[16] L. Librescu, S.-Y. Oh, J. Hohe, Linear and non-linear dynamic response of sandwich panels to blast loading, Composites B 35 (2004) 673–683.

[17] Y.Y. Yu, Forced flexural vibrations of sandwich plates in plane strain, J. Appl. Mech. 27 (1960) 535–540.

[18] P.C. Yang, C.H. Norris, Y. Stavsky, Elastic wave propagation in heterogeneous plates, Int. J. Solids Struct. 2 (1966) 665–684.

[19] C.T. Sun, J.M. Whitney, Forced vibrations of laminated composite plates in cylindrical bending, J. Acoust. Soc. Am. 55 (1974) 1003–1008.

[20] T. Anderson, E. Madenci, S.W. Burton, J.C. Fish, Analytical solutions to finite geometry composite panels under transient surface loading, Int. J. Solids Struct. 35 (1998) 1219–1239.

[21] H.J. Ding, D.J. Huang, H.M. Wang, Analytical solution for fixed-end beam subjected to uniform load, J. Zhejiang Univ. 6 (2005) 779–783.

[22] H.J. Ding, D.J. Huang, H.M. Wang, Analytical solution for fixed-fixed anisotropic beam subjected to uniform load, Appl. Math. Mech. (Engl. Ed.) 27 (2006) 1305–1310.

[23] H.J. Ding, D.J. Huang, W.Q. Chen, Elasticity solutions for plane anisotropic functionally graded beams, Int. J. Solids Struct. 44 (2007) 176–196.

[24] J.G. Ren, Bending theory of laminated plate, Compos. Sci. Technol. 27 (1986) 225–248.

[25] E. Carrera, Theories and finite elements for multilayered, anisotropic, composite plates and shells, Arch. Comput. Methods Eng. 9 (2002) 87–140.

[26] J.N. Reddy, Mechanics of Laminated Composite Plates, Theory and Analysis, CRC Press, 1997.

[27] K.S. Surana, R.K. Maduri, P.W. TenPas, J.N. Reddy, Elastic wave propagation in laminated composites using the space–time least-squares formulation in h, p, k framework, Mech. Adv. Mater. Struct. 13 (2006) 161–196.

[28] J.P. Pontaza, J.N. Reddy, Least-squares finite element formulation for shear-deformable shells, Comput. Methods Appl. Mech. Engrg. 194 (2004) 2464–2493.

[29] F. Moleiro, C.M. Mota Soares, C.A. Mota Soares, J.N. Reddy, Layerwise mixed least-squares finite element models for static and free vibration analysis of multilayered composite plates, Compos. Struct. 92 (2010) 2328–2338.

[30] G.M. Hulbert, T.J.R. Hughes, Space–time finite element methods for elastodynamics: formulations and error estimates, Comput. Methods Appl. Mech. Engrg. 66 (1988) 339–363.

[31] G.M. Hulbert, T.J.R. Hughes, Space–time finite element methods for second-order hyperbolic equations, Comput. Methods Appl. Mech. Engrg. 84 (1990) 327–348.

[32] R.D. Krieg, S.W. Key, Transient shell response by numerical time integration, Int. J. Numer. Methods Eng. 7 (1973) 273–286.

[33] S.W. Tsai, E.M. Wu, A general theory of strength for anisotropic materials, J. Compos. Mater. 5 (1971) 58–80.

[34] Z. Hashin, Failure criteria for unidirectional fiber composites, J. Appl. Mech. 47 (1980) 329–334.

[35] A. Puck, H. Schurmann, Failure analysis of FRP laminates by means of physically based phenomenological models, Compos. Sci. Technol. 58 (1998) 1045–1067.

[36] A.F. Bower, Applied Mechanics of Solids, Taylor and Francis, 2009.

[37] B. Alanbay, R.C. Batra, R.K. Kapania, Effect of extreme in-plane and transverse stiffness ratios on frequencies and load transfer between face sheets and core of rectangular sandwich plates, Compos. Struct. 278 (2020) Art. No. 114730.

[38] L. Yuan, R.C. Batra, Optimum first failure load design of one/two-core sandwich plates under blast loads, and their ultimate loads, Composite Structures 224 (2019) 111022.

[39] Lisha Yuan, Unchalisa Taetragool, Romesh C. Batra, Optimum first failure loads of one- and two-core doubly curved sandwich shells, AIAA J. 58 (2020) 3665–3679.